ROYAL SOCIETY
OF CHEMISTRY

PAPER

Check for updates

Structural, mechanical, dielectric properties and magnetic interactions in Dy³⁺-substituted Co–Cu–Zn nanoferrites

R. H. Kadam,[*a] R. B. Borade, [iD][b] M. L. Mane,[c] D. R. Mane,[d] K. M. Batoo[e]
and Sagar E. Shirsath [iD][*fg]

Sol–gel-synthesized Co–Cu–Zn ferrite nanoparticles diluted with Dy³⁺ ions were investigated in terms of their structural, morphological, elastic, magnetic and dielectric properties. X-ray diffraction patterns showed the formation of a single-phase cubic spinel structure. As the concentration of Dy³⁺ ions was increased, the lattice length gradually increased from 8.340 to 8.545 Å, obeying Vegard's law. The Williamson–Hall (W–H) method was employed to observe the change in the lattice strain. Crystallite size obtained from W–H plots followed a pattern similar to that observed using the Scherrer equation. The cation distribution suggested a strong preference of Dy³⁺ ions for the octahedral B site while Cu²⁺ and Fe³⁺ ions were distributed over both A and B sites. The microstructures of the samples were visualized using transmission electron microscopy. Mechanical properties such as stiffness constant, longitudinal and transverse wave velocities, Young's modulus, bulk modulus, rigidity modulus, Poisson's ratio and Debye temperature were investigated by acquiring infrared spectra recorded in the range of 300 to 800 cm⁻¹. Replacement of Fe³⁺ ions with the strongly magnetic Dy³⁺ ions increased the saturation magnetization and coercivity. Dielectric constant increased with Dy³⁺ substitution but decreased with applied frequency.

Introduction

Nanocrystalline spinel oxides such as ferrites display integral properties of magnetization and electrical insulation simultaneously and thus have attracted enormous attention of researchers and have prompted them to intensively investigate these systems. Ferrites offer numerous technological applications including telecommunications and electronic engineering, microwave-absorbing devices, transformer cores, magnetic recording media, magnetic resonance imaging, sensors, computer memory chips, ferro-fluids, radio frequency coil fabrication, catalysis, photocatalysis, magnetically guided drug delivery, hyperthermia, *etc.*[1–6] Nanodimension spinel

[a]*Materials Science Research Laboratory, Shrikrishna Mahavidyalaya, Gunjoti, Osmanabad, M.S., India. E-mail: ram111612@yahoo.co.in*

[b]*Department of Physics, MSS's Arts, Science and Commerce College, Ambad, Jalna, M.S., India*

[c]*Department of Physics, R. G. Shinde College, Paranda, Osmanabad, M.S., India*

[d]*Department of Higher Education, Maharashtra State, Central Building, Pune, M.S., India*

[e]*King Abdullah Institute for Nanotechnology, King Saud University, P.O. Box. 2455, Riyadh-1145, Saudi Arabia*

[f]*Department of Physics, Vivekanand College, Aurangabad, 431001, M.S., India. E-mail: shirsathsagar@hotmail.com*

[g]*School of Materials Science and Engineering, University of New South Wales, Sydney, NSW 2052, Australia*

ferrites constitute a primary class of nanomaterials having advantageous ferromagnetic properties that have promoted their technological applicability.[7–9] Among the ferrimagnetic spinel ferrites, $CoFe_2O_4$ with an $MgAl_2O_4$ inverse spinel-like crystal structure displays particularly excellent magnetic properties such as excellent saturation magnetization ($M_s \sim 80$ emu g⁻¹), coercivity ($H_c \sim 3$–5 kOe), first-order magnetocrystalline anisotropy constant ($K_1 \sim 10 \times 10^6$ erg cm⁻¹) and Curie temperature ($T_c \sim 870$ K).[10,11] Structural, elastic, magnetic and electrical properties of $CoFe_2O_4$ have been reportedly enhanced by the substitution of Cu and/or Zn ions.[1,12,13]

Apparently, properties of spinel ferrite have been shown to be modified by substitutions of rare earth (RE³⁺) ions at the octahedral B site.[14] These modifications have been attributed to the RE³⁺ ions having large magnetic moments, very large magnetostriction and large magnetocrystalline anisotropy as a result of their strong spin–orbit coupling of the angular momentum and unpaired 4f electrons.

Furthermore, the 4f shell of RE³⁺ ions is covered by $5s^2 5p^6$ electrons and is not influenced by the potential field of the neighbouring metal ions. The substitution of RE³⁺ into ferrites can establish the 4f–3d couplings that govern magnetocrystalline anisotropy and hence improve the magnetic properties of the ferrites.[15,16] Also, RE³⁺ oxides have good electrical resistivity of >10⁵ Ω cm at room temperature.[17,18] Among the RE³⁺ ions, substitution of Dy³⁺ ions have yielded particularly marked improvements in the

properties of ferrites.[19,20] In the current work, the structural, elastic, magnetic and dielectric properties of $Co_{0.4}Cu_{0.1}Zn_{0.5}Dy_xFe_{2-x}O_4$ (where, $x = 0.0, 0.015, 0.03, 0.045$) nanoparticles synthesized using the sol–gel auto-combustion route were revealed, for the first time to the best of our knowledge.

The sol–gel auto-combustion method was used in the present work for the synthesis of $Co_{0.4}Cu_{0.1}Zn_{0.5}Dy_xFe_{2-x}O_4$ materials since use of this method has been shown to produce nanoparticles. Importantly, relative to other available processes such as co-precipitation and hydrothermal methods, the sol–gel auto-combustion method displays advantages such as the ability to form a desired phase and composition, control over crystal size and aggregation state, short processing time, easy process, and use of inexpensive raw materials.[1]

The main objective of the present work was to investigate the effect of Dy^{3+} ions on the structural, optical and magnetic properties of the Co–Cu–Zn ferrite. Regarding structural properties, the crystallite size and strain effect were investigated systematically. Elastic behavior was investigated using infrared spectroscopy. Magnetic properties such as saturation magnetization and coercivity of the investigated samples were also studied for their possible applications in technological devices.

Materials and methods

Pure, ultrafine nanopowders of $Co_{0.4}Cu_{0.1}Zn_{0.5}Dy_xFe_{2-x}O_4$ ($x = 0.0, 0.015, 0.03, 0.045$) were fabricated by applying the sol–gel autocombustion method. Ultrapure ((>99%) metal nitrates of $Co(NO_3)_2 \cdot 6H_2O$, $Cu(NO_3)_2 \cdot 6H_2O$, $Zn(NO_3)_2 \cdot 6H_2O$, $Fe(NO_3)_3 \cdot 9H_2O$, and $Dy(NO_3)_3 \cdot 9H_2O$ were used in combination with $(C_6H_8O_7 \cdot H_2O)$ as a chelating agent in the molar ratio of 1 : 3. Liquid ammonia was slowly introduced into the solution in order to adjust the pH to be $\cong 7$. Until a viscous gel formed, the whole mixture was continuously stirred at a constant temperature of 90 °C. After a self-ignition process was carried out, the burnt powders were sintered at 700 °C for 6 h and ground in order to obtain the desired fine nanoparticles.

Powder samples were characterized by subjecting them to X-ray diffraction analysis using a Rigaku (*Miniflux II*) diffractometer spanning diffraction angles from $20-80°$ at a slow rate of $2°$ per minute together with using Cu-K$_\alpha$ radiation ($\lambda = 1.5406$ Å) at 40 kV. The microstructures and surface morphologies of the samples were investigated using transmission electron microscopy (JEOL JEM 2100). Elasticity parameters were computed from FTIR spectra recorded in the range $300-800$ cm^{-1}. FTIR measurements were performed on disc-shaped samples made by using ferrite-KBr with a ratio of 1 : 10. Magnetic characterization was carried out using a vibrating sample magnetometer and applying a magnetic field of up to 5 kOe. The dielectric behavior of the samples was investigated by first forming silver-pasted discs of them and then analyzing the discs by using a Hioki HiTESTER 3532-50.

Results and discussion

Structural analysis

Bragg reflections from the (220), (311), (222), (400), (422), (333), (440), and (533) planes (indexed by ICCD # 00-008-0234) were observed in the X-ray diffraction (XRD) patterns of $Co_{0.4}Cu_{0.1}Zn_{0.5}Dy_xFe_{2-x}O_4$ (Fig. 1). These patterns clearly indicated the formation of a single phase, in particular a cubic spinel structure belonging to the space group $Fd\bar{3}m$.[23] Neither any impurity nor a secondary phase was indicated from an analysis of the XRD patterns. Addition of Dy^{3+} ions shifted the peak positions of $Co_{0.4}Cu_{0.1}Zn_{0.5}Fe_2O_4$ slightly towards the lower angles, as depicted in Fig. 1. The experimental lattice length a_{exp} was computed by employing the equation[21] $a_{exp} = d\sqrt{h^2 + k^2 + l^2}$, where $(h\ k\ l)$ are the Miller indices and d is the interplanar distance. As shown in Fig. 2a, the lattice length of $Co_{0.4}Cu_{0.1}Zn_{0.5}Dy_xFe_{2-x}O_4$ increased from 8.340 to 8.545 Å with the substitution of Dy^{3+} ions. This change in a_{exp} can be understood in terms of the ionic radii of the constituent ions, where Fe^{3+} ions of smaller ionic radii (0.67 Å) were replaced with Dy^{3+} ions of greater ionic radii (0.99 Å). The observed increase in a_{exp} indicated the substitution of Dy^{3+} ions into $Co_{0.4}Cu_{0.1}Zn_{0.5}Fe_2O_4$ possibly inducing tensile strain into the lattice by deforming it elastically.

The nanocrystalline nature of the samples obtained from the Debye–Scherrer relationship and the microstrain induced in the crystal lattice were studied by using the Williamson–Hall (W–H) relationship[22]

$$\beta \cos \theta = \frac{C\lambda}{D_{W-H}} + 4\varepsilon \sin \theta, \quad (1)$$

where $C = 0.94$ for the nanocrystals of uniform size, D_{W-H} is the crystallite size, λ is incident wavelength, and ε is the microstrain induced in the crystal lattice. In comparison to the Debye–Scherrer relationship, W–H analysis gives better information about crystallite size.[23] Values of ε and D_{W-H} were obtained from the slope and y-intercept of the fitted line drawn between $4 \sin \theta$ and $\beta \cos \theta$ as shown in Fig. 3. Strain values are given in the inset of Fig. 3 and D_{W-H} values for various Dy concentrations are shown in Fig. 2b. D_{W-H} obtained from W–H plots were observed to range from 31.76 to 34.40 nm for the tested concentrations, and the strain values ranged from 3.133×10^{-4} to 4.344×10^{-4}.
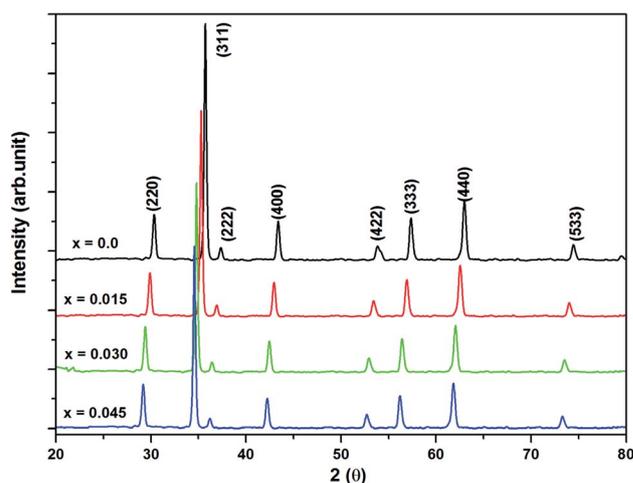

Fig. 1 X-ray powder diffraction patterns of all of the investigated samples of $Co_{0.4}Cu_{0.1}Zn_{0.5}Dy_xFe_{2-x}O_4$.
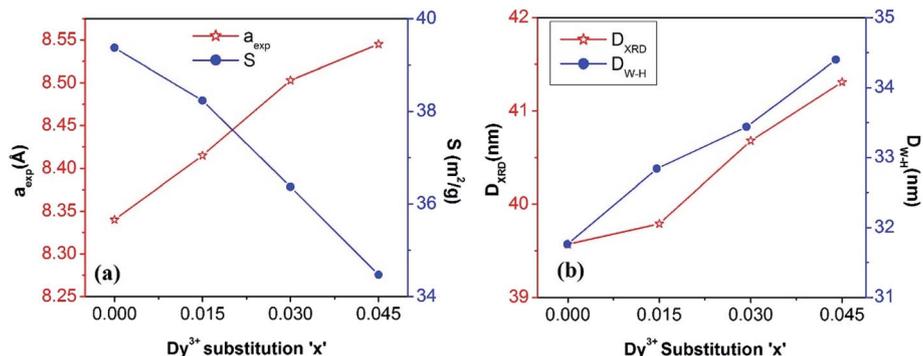
Fig. 2 (a) Experimental lattice length (a_{exp}) and specific surface area (s) values and (b) crystallite sizes obtained from XRD (D_{XRD}) and from W−H plots (D_{W-H}) of $Co_{0.4}Cu_{0.1}Zn_{0.5}Dy_xFe_{2-x}O_4$ ferrites.

Positive values of slope here indicated that the tensile type of strain induced on the lattice increased with the Dy substitution. The increase in tensile strain with Dy substitution was also consistent with the observed change in the lattice length described above.

The crystallite diameter D_{XRD} of the powders was also obtained by using the peak broadening (β) and Bragg angle (θ) of the (311) peak from the well-known Debye–Scherrer[23] equation $D_{XRD} = (C\lambda/\beta \cos \theta)$, where $C = 0.94$ and $\lambda = 1.5406 \times 10^{-10}$ m. Addition of Dy^{3+} ions into Co–Cu–Zn ferrites increased the D_{XRD} from 39.57 to 41.31 nm (Fig. 2b). The specific surface area (S) was computed by using the relationship[24]

$$S = \frac{6}{d_X D_{XRD}}, \qquad (2)$$

where d_X is X-ray density and 6 is the shape factor. As shown in Fig. 2a, S decreased from 39.37 $m^2\ g^{-1}$ to 34.47 $m^2\ g^{-1}$ as Dy was substituted. This decrease was related to the increased D_{XRD} of the samples with Dy substitution.

Cation distribution

The Bertaut method[25] was adopted to compute the cation distribution in $Co_{0.4}Cu_{0.1}Zn_{0.5}Dy_xFe_{2-x}O_4$. When using this method, a few pairs of the most sensitive reflections were selected according to the expression $(I_{hkl}^{Obs.}/I_{h'k'l'}^{Obs.}) = (I_{hkl}^{Cal.}/I_{h'k'l'}^{Cal.})$, where $I_{hkl}^{Cal.}$ and $I_{hkl}^{Obs.}$ denote the calculated and observed intensities, respectively. Cation distribution was obtained by comparing the ratios of calculated and experimental intensities for the (220), (400) and (440) reflections. These reflections have been shown (i) to be not dependent on oxygen, (ii) to have similar intensities, (iii) to have intensities varying inversely with cation occupancy. The corresponding integrated intensity I_{hkl} was evaluated by using the relationship derived by Buerger,[26,27] namely
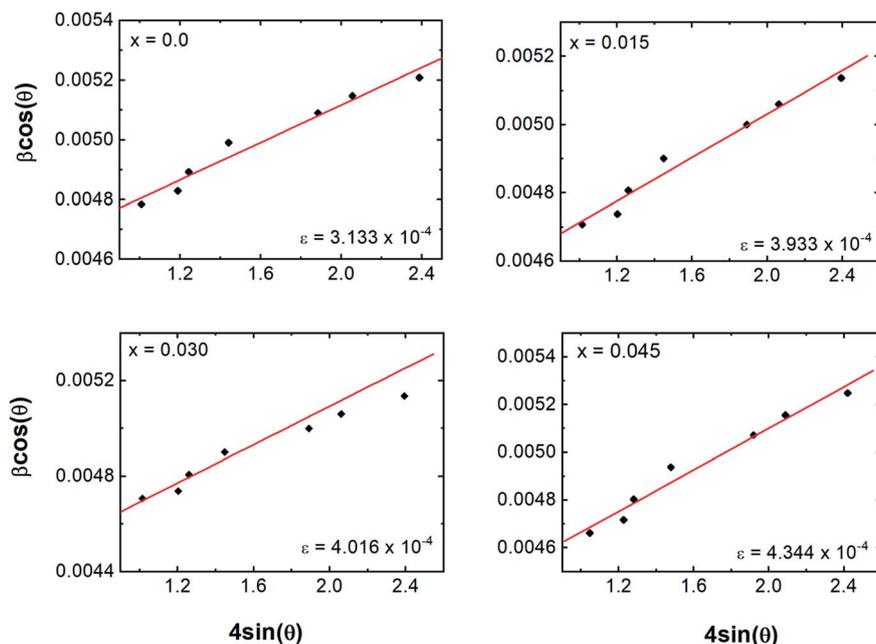

Fig. 3 Williamson–Hall analysis plots of $\beta \cos \theta$ versus $4 \sin \theta$ of $Co_{0.4}Cu_{0.1}Zn_{0.5}Dy_xFe_{2-x}O_4$.

$$I_{hkl} = |F|_{hkl}^2 PL_P, \qquad (3)$$

where L_P, P and F denote the Lorentz polarization, multiplicity and structure factor, respectively. L_P was obtained by using the relationship[23]

$$L_P = \frac{1 + \cos^2 2\theta}{\sin^2 \cos \theta}. \qquad (4)$$

The cation distribution of $Co_{0.4}Cu_{0.1}Zn_{0.5}Dy_xFe_{2-x}O_4$ spinel ferrite system obtained using the XRD technique is depicted in Table 1. Cu^{2+} ions occupied tetrahedral A site and octahedral B site. Zn^{2+} ions showed a preference for the A site whereas Co^{2+} ions occupied the B site. Dy^{3+} occupied the octahedral B site by replacing Fe^{3+} from the octahedral sites, a result consistent with the high B-site energy of RE^{3+} ions.

Cation distribution data of $Co_{0.4}Cu_{0.1}Zn_{0.5}Dy_xFe_{2-x}O_4$ and ionic radii of constituent ions therein were used to determine values for the ionic radius of the A site, abbreviated as r_A, and that of the B site, i.e., r_B. As shown in Fig. 4a, r_A and r_B both increased with the Dy^{3+} substitution, attributed to the larger ionic radii of Dy ions compared to those of the Fe ions. The oxygen parameter u was obtained from the oxygen ion radius R_O (1.32 Å) and r_A using the equation:[27]

$$u = \left[(r_A + R_0) \frac{1}{\sqrt{3a}} + \frac{1}{4} \right]. \qquad (5)$$

As shown in Fig. 4b, u decreased from 0.3882 Å to 0.3877 Å with the Dy substitution. According to many researchers, u would be expected to be 0.250 Å for the origin at the octahedral sites, and about 0.375 Å for the origin at tetrahedral sites and a centric crystal structure.[28,29] According to XRD studies of some researchers, $u > 0.375$ Å for substituted ferrites.[29,30] In the present study, u was determined to be higher than its expected "ideal" value of 0.375 Å.

The theoretical lattice length, a_{th}, was determined using the relationship[31]

$$a_{th} = \frac{8}{3\sqrt{3}} \left[(r_A + R_0) + \sqrt{3} (r_B + R_0) \right]. \qquad (6)$$

As shown in Fig. 4c, a_{th} increased from 8.543 to 8.563 Å with the Dy^{3+} substitution in $Co_{0.4}Cu_{0.1}Zn_{0.5}Fe_2O_4$ ferrite.

Shared and unshared octahedral edges (d_{BXE} and d_{BXEU}), the tetrahedral edge (d_{AXE}) and tetrahedral and octahedral bond lengths (d_{AX} and d_{BX}) were obtained using relationships discussed elsewhere. As shown in Fig. 4d, d_{BXE}, d_{BXEU}, d_{AX}, d_{BX} and d_{AXE} increased with the Dy^{3+} substitution. Such a change was ascribed to the increase in the value of a_{exp} of $Co_{0.4}Cu_{0.1}Zn_{0.5}Fe_2O_4$ with Dy^{3+} substitution.

Transmission electron microscopy

Fig. 5a and b depict the transmission electron microscopy images of the $x = 0.0$ and $x = 0.045$ samples, respectively. TEM images revealed the homogeneity of the sol–gel-synthesized samples with uniform particle size distribution. Most of the particles showed spherical shapes, in accordance with the tendency of cubic crystals to form spherical shapes in order to minimize surface tension.[32,33] The agglomerations observed in the particles may be related to the interactions of magnetic dipoles arising within the ferrite nanoparticles.[34] The main purpose of our acquiring the TEM images was to estimate the particle size, which was measured by employing ImageJ software (Version 1.52V). Fig. 5c and d show the histograms of the particle size distribution for the $x = 0.0$ and $x = 0.45$ samples, respectively. For the $x = 0.0$ sample, the particle sizes were observed to be in the range 28.53 to 97.16 nm with an average value of 62.632 nm. For the $x = 0.045$ sample, the particle sizes were observed to be in the range 41.97 to 114.215 nm with an average value of 77.789 nm.

Elastic properties

Infrared spectra spanning wavenumbers of 300–800 cm^{-1} were obtained for the $Co_{0.4}Cu_{0.1}Zn_{0.5}Dy_xFe_{2-x}O_4$ samples (Fig. 6). The vibration bands observed in the vicinity of $\nu_A \sim 585$ cm^{-1} and $\nu_B \sim 375$ cm^{-1} were related to the stretching vibrations of metal ion and oxygen bond at the A and B sites, respectively, which confirmed that the powders crystallized in the cubic spinel structure.[35]

For the present series, ν_A and ν_B varied with the Dy^{3+} ions substitution in $Co_{0.4}Cu_{0.1}Zn_{0.5}Fe_2O_4$ (Table 2). The insertion of Dy^{3+} ions was seen to shift ν_A and ν_B slightly towards higher frequencies. This shifting of absorption bands was ascribed to the crystallite size[35] and cation occupancy. The force constant of the A site, denoted as K_T, and that of the B site, denoted as K_O, were estimated by employing relationships discussed elsewhere.[36] K_T and K_O were computed by using the positions of the

Table 1 Distributions of cations at the tetrahedral A site and octahedral B site and intensity ratios for $Co_{0.4}Cu_{0.1}Zn_{0.5}Dy_xFe_{2-x}O_4$

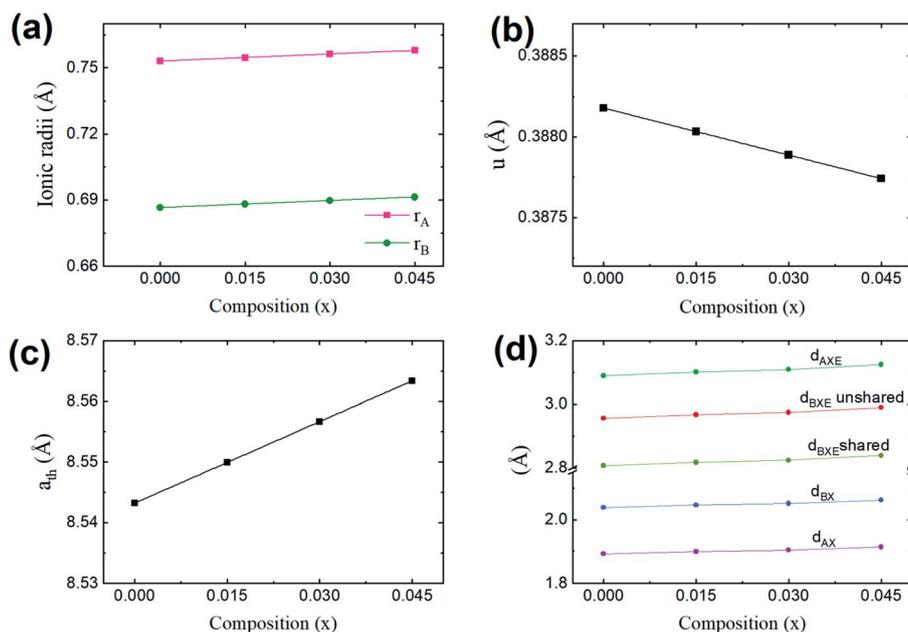| Comp. x | Cation distribution | | Intensity ratios | | | |
| | | | (220/440) | | (440/422) | |
	A site	B site	Obs.	Cal.	Obs.	Cal.
0.0	$Cu_{0.05}Zn_{0.5}Fe_{0.45}$	$Cu_{0.05}Co_{0.4}Fe_{1.55}$	0.692	0.701	3.957	4.094
0.015	$Cu_{0.05}Zn_{0.5}Dy_{0.005}Fe_{0.445}$	$Cu_{0.05}Co_{0.4}Dy_{0.01}Fe_{1.54}$	0.709	0.714	4.056	4.073
0.03	$Cu_{0.05}Zn_{0.5}Dy_{0.01}Fe_{0.44}$	$Cu_{0.05}Co_{0.4}Dy_{0.02}Fe_{1.53}$	0.708	0.729	4.069	4.043
0.045	$Cu_{0.05}Zn_{0.5}Dy_{0.015}Fe_{0.435}$	$Cu_{0.05}Co_{0.4}Dy_{0.03}Fe_{1.52}$	0.716	0.736	4.056	4.024

Fig. 4 (a) Values of the mean ionic radii at the tetrahedral A site (r_A) and octahedral B site (r_B), (b) oxygen positional parameter (u), (c) theoretical lattice length (a_{th}) and (d) allied parameters such as; tetrahedral bond (d_{AX}), octahedral bond (d_{BX}), tetrahedral edge (d_{AXE}), and octahedral edge (d_{BXE}) shared and unshared, for the $Co_{0.4}Cu_{0.1}Zn_{0.5}Dy_xFe_{2-x}O_4$ ferrites.

high- and low-frequency bands ν_A and ν_B and are presented in Table 2. The average force constant was obtained using the expression $K_{av} = (K_O + K_T)/2$, and the values are given in Table 2.

Force constants obtained from infrared spectra and the crystallographic parameters were used to calculate the stiffness constant and various elastic parameters. According to
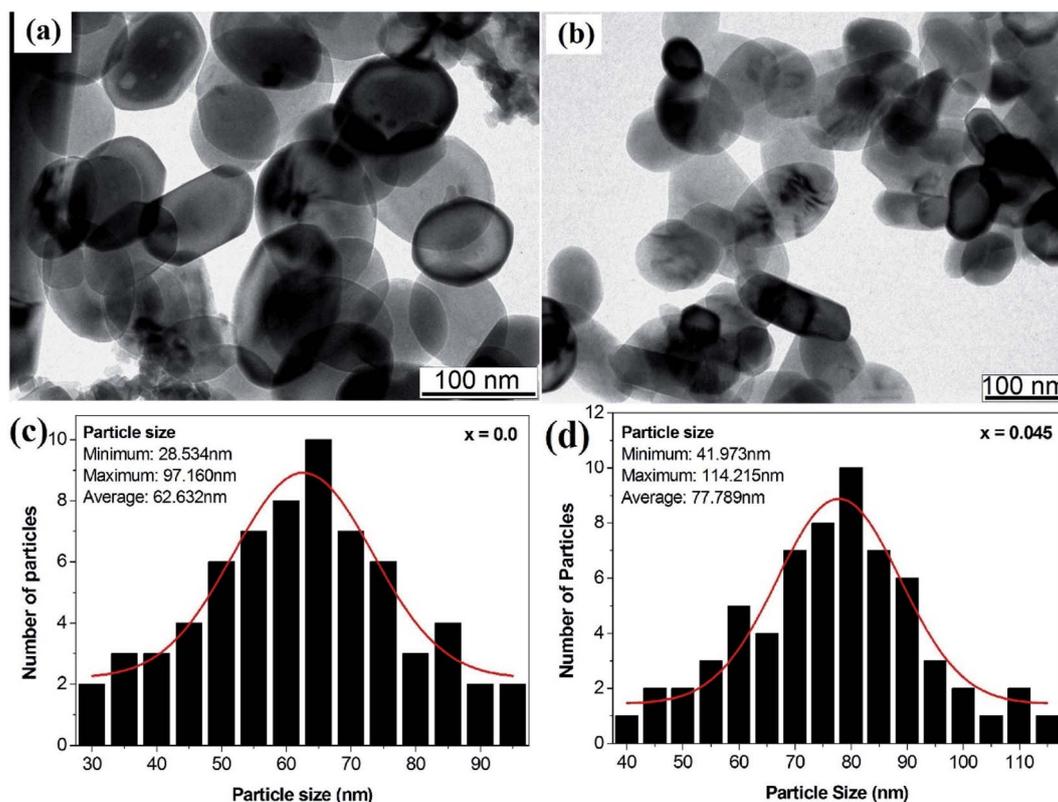

Fig. 5 (a) TEM image of the $x = 0.0$ sample, (b) TEM image of the $x = 0.045$ sample, and (c) histogram of the particle size distribution for the $x = 0.0$ sample and (d) histogram of the particle size distribution for the $x = 0.045$ sample of the $Co_{0.4}Cu_{0.1}Zn_{0.5}Dy_xFe_{2-x}O_4$ ferrites.
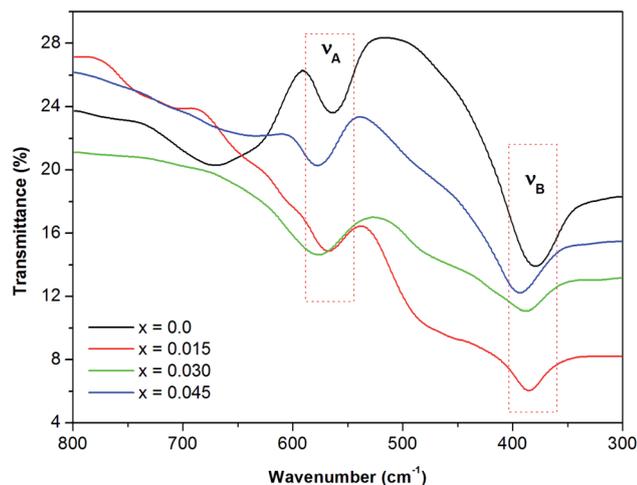
Fig. 6 Infrared spectra of all of the investigated samples of the $Co_{0.4}Cu_{0.1}Zn_{0.5}Dy_xFe_{2-x}O_4$ ferrites.

Table 2 Band positions (ν_A and ν_B), force constants (K_T, K_O and K_{av}), elastic parameters such as stiffness constant (C_{11}), longitudinal wave velocity (V_l), transverse wave velocity (V_t), bulk modulus (B), rigidity modulus (G), Poisson's ratio (σ), Young's modulus (E), mean wave velocity (V_m) and Debye temperatures (θ_D) obtained using the Waldron and Anderson methods for $Co_{0.4}Cu_{0.1}Zn_{0.5}Dy_xFe_{2-x}O_4$

Comp. 'x'	0.0	0.015	0.030	0.045
ν_A (cm^{-1})	564.19	567.08	575.76	577.69
ν_B (cm^{-1})	379.02	384.81	387.70	393.49
K_T ($\times 10^5$ dynes per cm)	195.49	198.81	206.29	209.03
K_O ($\times 10^5$ dynes per cm)	120.30	124.84	127.58	132.29
K_{av} ($\times 10^5$ dynes per cm^{-1})	157.90	161.82	166.93	170.66
C_{11} (GPa)	189.32	192.30	196.32	199.72
V_l (m s^{-1})	5889.60	5996.52	6133.83	6211.11
V_t (m s^{-1})	3400.36	3462.09	3541.37	3585.99
B (GPa)	189.32	192.30	196.32	199.72
G (GPa)	63.11	64.10	65.44	66.57
σ	0.35	0.35	0.35	0.35
E (GPa)	170.39	173.07	176.69	179.75
V_m (m s^{-1})	3775.04	3843.58	3931.59	3981.13
Θ_D (K) (Waldron)	678.17	684.41	692.73	698.28
θ_D (K) (Anderson)	539.17	544.03	550.72	554.97

Waldron,[35] stiffness constant $C_{11} = C_{12}$ for the materials possessing the cubic spinel crystal structure and is given by the equation $C_{11} = K_{av}/a$. Various elasticity parameters such as rigidity modulus G, bulk modulus B, Young's modulus E, longitudinal wave velocity V_l, transverse wave velocity V_t, mean wave velocity V_m and Poisson's ratio σ were calculated by using the relationships[37]

$$B = \frac{1}{3}(C_{11} + 2C_{12}), \tag{7}$$

$$V_l = (C_{11}/\rho)^{1/2}, \tag{8}$$

$$V_t = V_l/3, \tag{9}$$

$$G = \rho V_t 2, \tag{10}$$

$$\sigma = \frac{3B - 2G}{6B + 2G}, \tag{11}$$

$$E = (1 + \sigma)2G, \tag{12}$$

and

$$V_m = \left[\frac{1}{3}\left(\frac{2}{V_t^3} + \frac{1}{V_l^3}\right)\right]^{-1/3}, \tag{13}$$

The changes in the various elasticity parameters and modulus with Dy^{3+} being substituted into the Co–Cu–Zn ferrite system are presented in Table 2. Stiffness constant C_{11} and all elastic moduli (B, G, and E) increased with the addition of Dy^{3+} ions into the Co–Cu–Zn ferrites. Poisson's constant was indeed constant ($\sigma = 0.35$) for all of the investigated compositions. According to isotropic elasticity theory[35,38,39] and literature reports, Poisson's ratio must be in the range -1 to 0.5 in order to achieve good elastic behaviour. In general, elastic moduli values are related to the interionic bonding. As suggested by A. Bhaskar,[40] strong bonding between the ions would enhance the values of the elastic moduli. In the present case, the increasing values of the elastic moduli with the addition of Dy^{3+} ions could ascribed to the increasing interatomic bonding between the ions of the Dy^{3+}-substituted Co–Cu–Zn ferrites.

Debye temperatures (θ_D) values of all of the investigated compositions were estimated from the relationship suggested by Anderson,[41] namely

$$\theta_D = \frac{h}{k_B} \times V_m \left[\frac{3n\rho N_A}{4\pi M}\right]^{1/3}, \tag{14}$$

where k and h are Boltzmann's and Planck's constants, respectively, N_A is Avogadro's number, n is the number of atoms per unit cell (for cubic spinel, $n = 8$), ρ denotes density, V_m is the mean wave velocity, and M is the molecular weight. The Debye temperature can also be obtained by using the relationship suggested by Waldron,[35] namely

$$\Theta_D = \frac{\hbar C}{k_B}\nu_{av} = 1.438 \times \nu_{av}, \tag{15}$$

where ν_{av} is the average of the absorption bands (ν_A, ν_B) and is given by $\nu_{av} = (\nu_A + \nu_B)/2$. Both values of Debye temperatures obtained from the relationships suggested by Anderson and Waldron are given in Table 2. Addition of Dy^{3+} ions increased θ_D from 539.17 to 554.97 K and Θ_D from 678.17 to 698.28 K. The change in Debye temperature may be understood based on the theory of specific heat.[42] Increasing P-type conduction in the materials may have increased the Debye temperature. Also, the increased rigidity of the Dy^{3+}-doped Co–Cu–Zn ferrites may have contributed to its increased Debye temperature.

The elastic moduli (B, G and E) are not reliable unless the correction made to the zero porosity, which can be obtained by the void fraction (P) using the Hosselmann and Fulrath formula[40]

Table 3 Void-free corrected values of elastic parameters, including Poisson's ratio (σ_0), rigidity modulus (G_0), Young's modulus (E_0) and bulk modulus (B_0), for $Co_{0.4}Cu_{0.1}Zn_{0.5}Dy_xFe_{2-x}O_4$

Comp. 'x'	0.0	0.015	0.030	0.045
E_0 (GPa)	198.07	203.55	210.27	216.48
G_0 (GPa)	72.54	74.47	76.86	79.05
B_0 (GPa)	254.08	254.29	265.30	275.95
σ_0	0.365	0.367	0.368	0.369

$$E_0 = \left[\frac{1}{E}\left\{1 - \frac{3P(1-\sigma)(9+5\sigma)}{2(7-5\sigma)}\right\}\right]^{-1}, \quad (16)$$

$$G_0 = \left[\frac{1}{G}\left\{1 - \frac{15P(1-\sigma)}{(7-5\sigma)}\right\}\right]^{-1}, \quad (17)$$

$$B_0 = \frac{E_0 G_0}{3(3G_0 - E_0)}, \quad (18)$$

and

$$\sigma_0 = \frac{E_0}{2G_0} - 1. \quad (19)$$

Void-free corrected values of Poisson's ratio (σ_0), rigidity modulus (G_0), Young's modulus (E_0) and bulk modulus (B_0) are presented in Table 3. All of these elastic moduli of Co–Cu–Zn ferrites tended to increase with the increasing amount of substituted Dy^{3+} ions, consistent with above-described corresponding strengthening of the bonding between the corresponding ions.

Magnetic properties

In general, three magnetic interactions such as A–A, A–B and B–B take place between the cations and neighboring anions in spinel ferrites through a super-exchange mechanism. The strengths of the energies of interaction between the magnetic ions (Me^I and Me^{II}) are related to the cation–anion bond lengths and the Me^I–O–Me^{II} angle (θ). Apparently, in general,

the length of the A–B bond is less than that of the A–A bond. Thus, an A–B super-exchange interaction would be stronger than A–A and B–B super-exchange interactions. The maximum angle θ of 180° connecting the cations would result in the highest interaction energy. The cation–anion (Me^I–O) (p, q, r, and s) and cation–cation (Me^I–Me^{II}) (b, c, d, e, and f) interionic distances, and bond angles (θ_1, θ_2, θ_3, θ_4, and θ_5) for the cations and cation–anion, were determined by using the equations listed in Table 4.[43] Fig. 7a–c show that the cation distances, Me^I–Me^{II}, increased with an increasing amount of Dy substituted in the Co–Cu–Zn ferrite. In the case of distances between the cation and anion, namely Me^I–O, P and S increased whereas Q and R decreased with an increasing amount of Dy substituted. The substitution of larger Dy^{3+} ions for Fe^{3+} ions at the BO_6 octahedral site resulted in an increased bond length. As shown Fig. 7c, the angles associated with the A–B interaction (θ_1 and θ_2) increased, those associated with the B–B interaction (θ_3 and θ_4) decreased, and that associated with the A–A interaction (θ_5) increased by small margin with an increasing amount of Dy^{3+} substituted. The variation in bond angles revealed that A–O–B interaction, which governs the magnetization in the system, strengthened with an increasing amount of Dy ions substituted. Such a change should increase the magnetization levels of the Co–Cu–Zn ferrites. Thus magnetic properties were investigated by employing VSM with a peak field strength of 5 kOe. Fig. 8a presents the magnetic hysteresis loops obtained from our system; these loops clearly indicated that the saturation magnetization (M_s) increased with increases in Dy^{3+} concentration. The RE-Dy^{3+} ions showed a greater magnetic moment (10.48 μ_B) compared to that of Fe^{3+} (5 μ_B). The increased content of Dy^{3+} ions at the B sites increased the magnetization of these sites, which resulted in the increase in the M_s.

Coercivity (H_c) is generally governed by the magnetocrystalline anisotropy constant (K_1), permeability (μ_O) and M_s through the Brown relationship[44]

$$H_C = \frac{2K_1}{\mu_0 M_S}. \quad (20)$$

Table 4 Expressions for determining the interionic distances for the cation–cation (Me^I–Me^{II} (b, c, d, e, and f), cation–anion Me^I–O (p, q, r, and s), and bond angles (θ_1, θ_2, θ_3, θ_4, and θ_5)

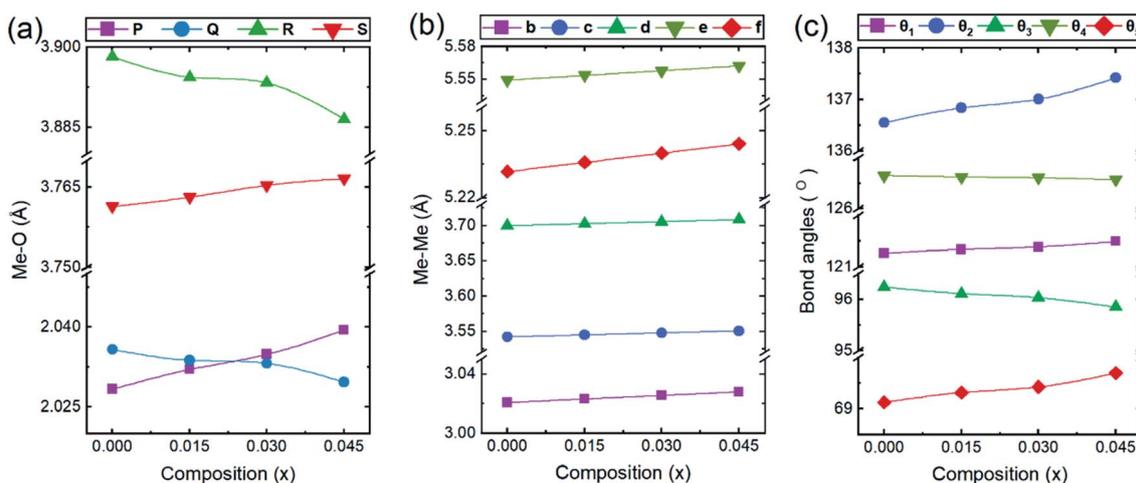| Me^I–Me^{II}	Me^I–O	Bond angles
$b = \sqrt{2}\left(\frac{a}{4}\right)$	$p = a\left(\frac{1}{2} - u^{3m}\right)$	$\theta_1 = \cos^{-1}\left(\frac{p^2 + q^2 - c^2}{2pq}\right)$
$c = \sqrt{11}\left(\frac{a}{11}\right)$	$q = a\sqrt{3}\left(u^{3m} - \frac{1}{8}\right)$	$\theta_2 = \cos^{-1}\left(\frac{p^2 + r^2 - e^2}{2pr}\right)$
$d = \sqrt{3}\left(\frac{a}{4}\right)$	$r = a\sqrt{11}\left(u^{3m} - \frac{1}{8}\right)$	$\theta_3 = \cos^{-1}\left(\frac{2p^2 - b^2}{2p^2}\right)$
$e = 3\sqrt{3}\left(\frac{a}{8}\right)$	$s = a\sqrt{3}\left(u^{3m} + \frac{1}{8}\right)$	$\theta_4 = \cos^{-1}\left(\frac{p^2 + s^2 - f^2}{2ps}\right)$
$f = \sqrt{6}\left(\frac{a}{4}\right)$		$\theta_5 = \cos^{-1}\left(\frac{r^2 + q^2 - d^2}{2rq}\right)$

Fig. 7 The calculated values of (a and b) the interionic distances for the (a) cation–anion Me^I–O (p, q, r, and s), (b) cation–cation Me^I–Me^{II} (b, c, d, e, and f), and (c) bond angles (θ_1, θ_2, θ_3, θ_4, and θ_5).

The coercivity value is independent of M_s and can be controlled by heat treatment or structural deformation. Values of M_s, H_c, remnant magnetization (M_r) and remanence ratio ($R = M_r/M_s$), each as a function of the relative amount of Dy^{3+} substituted, are shown in Fig. 9a–d. As shown in Fig. 8b and 9c, H_c increased with increasing amount Dy^{3+} substituted. An increased H_c is in general directly related to the higher K_1 of rare earth ions such as Dy.

In general, cation distribution, particle sizes and magnetic moments of the cations are the major parameters affecting magnetic properties. However, oxygen vacancies and variation in the valence state of Fe, namely between Fe^{3+} and Fe^{2+}, can also influence the magnetic properties.[10] However, in the present case, all of the materials were sintered in an air atmosphere and thus the possibility of having oxygen vacancies can be neglected. Secondly, the Dy and Fe ions in the materials used had the same valence state of 3+. Considering these factors, a change in the valence state between Fe^{3+} and Fe^{2+} can be ignored in the present work, though it can be studied in the future using XPS.

Dielectric measurements

The dielectric constant (ε') was obtained using a cylindrical ferrite pellet sample and the relationship

$$\varepsilon' = \frac{C_p d}{\varepsilon_0 A},\qquad(21)$$

where d is the pellet thickness, C_p is the capacitance, A is the area of pellet surface and ε_0 is the permittivity of free space. Fig. 10a and b show dielectric constant (ε') and dielectric loss tangent (tan δ) values, each as a function of frequency. These two values decreased with increasing frequency, confirming the dispersion at lower frequency.[45] The dispersion and higher value of ε' at low frequency may be ascribed to the grain heterogeneity of material.[46] The change in dielectric dispersion can be understood via the Maxwell–Wagner model[47,48] and Koop's[49] phenomenological theory. The exchange of 3d orbital electrons between Fe^{2+} and Fe^{3+} can be localized at the metal ions, resulting in a local shift of electrons (e^-) toward the direction of the applied electric field and helping to determine
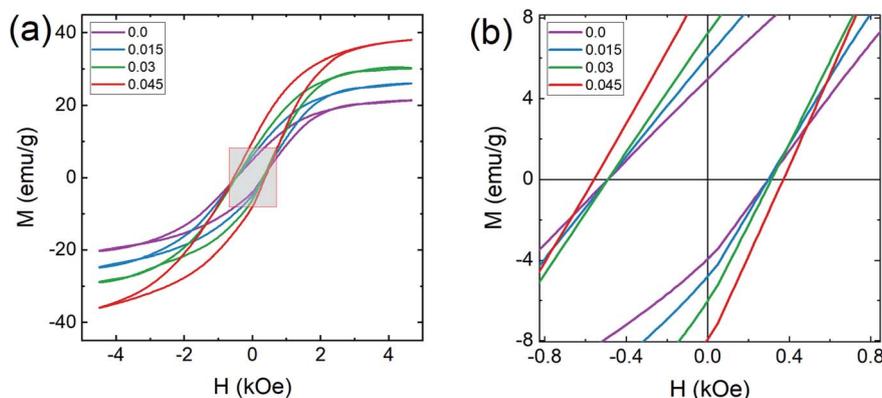

Fig. 8 Magnetization curves of $Co_{0.4}Cu_{0.1}Zn_{0.5}Dy_xFe_{2-x}O_4$. (a) Magnetization ($M$) as a function of applied magnetic field (H) and (b) expanded view of the M–H plots at low applied magnetic field strengths.
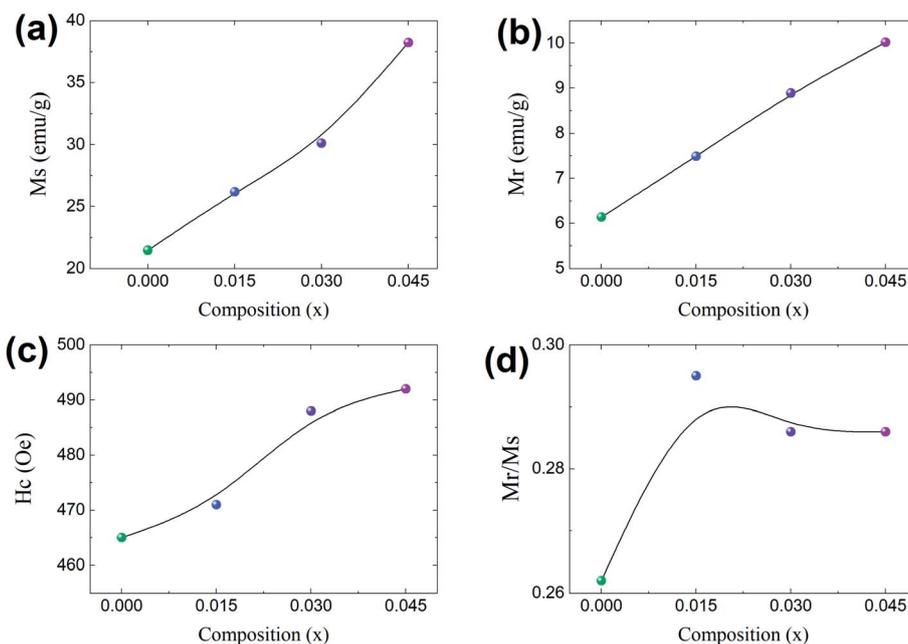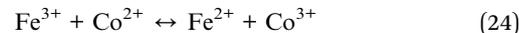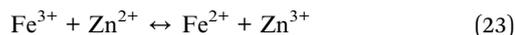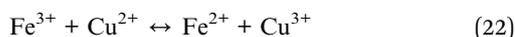
Fig. 9 $Co_{0.4}Cu_{0.1}Zn_{0.5}Dy_xFe_{2-x}O_4$ magnetism properties each as a function of Dy composition (x). (a) Magnetization (M_s), (b) remnant magnetization (M_r), (c) coercivity (H_c), and (d) the remnant ratio M_r/M_s.

the polarization strength. The variation in ε' and tan δ at low frequency may also be related to the 'grain-boundary-induced high resistivity'. Thus more energy is needed at the low-frequency region for the exchange of electrons between Fe^{2+} and Fe^{3+} ions, which gives higher values of ε' and tan δ. In contrast, at the higher-frequency region, dispersion is related to 'grain-induced lower resistivity'. Thus, less energy is needed for inter-cation electron exchange. Furthermore, a higher tan δ at lower frequency may be related to crystal defects, impurities and moisture. The conduction of Cu^{2+}, Co^{2+}, Zn^{2+} with Fe^{3+} ions at the B site is possible through following mechanisms:

$$Fe^{3+} + Cu^{2+} \leftrightarrow Fe^{2+} + Cu^{3+} \quad (22)$$

$$Fe^{3+} + Zn^{2+} \leftrightarrow Fe^{2+} + Zn^{3+} \quad (23)$$

$$Fe^{3+} + Co^{2+} \leftrightarrow Fe^{2+} + Co^{3+} \quad (24)$$

The value of tan δ reflects the energy loss within a material and it appears whenever polarization does not follow the applied alternating field. A broad relaxation-related hump in each of the tan δ plots was observed (Fig. 10b) and can be understood based on the Rezlescu model.[50] The condition for a broad hump in the tan δ of a dielectric material is related to the equation

$$\omega\tau = 1, \quad (25)$$

where τ is the relaxation time and $\omega = 2\pi f_{max}$. The value of τ is related to the jumping probability according to the relationship

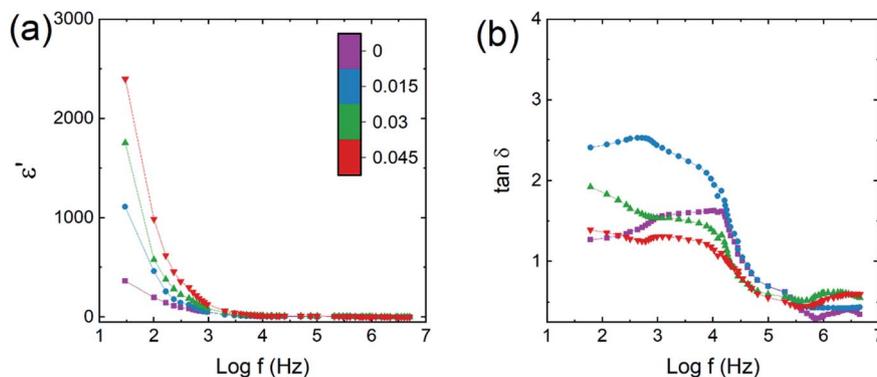Fig. 10 $Co_{0.4}Cu_{0.1}Zn_{0.5}Dy_xFe_{2-x}O_4$ dielectric parameters, each as a function of logarithm of frequency (f). (a) Real part of dielectric constant (ε') and (b) dielectric loss tangent (tan δ).

$$\tau = \frac{1}{2p} \tag{26}$$

or

$$f_{\max} \propto p \tag{27}$$

Thus, a broad hump or maximum can be obtained as a result of frequency of charge hopping between cations perfectly coinciding with the frequency of the electric field. The Co–Cu–Zn ferrite samples with $x = 0.045$ showed the highest ε' and lowest $\tan \delta$.

The increase in ε' for Co–Cu–Zn ferrite with increasing amount of Dy^{3+} substituted could be mainly related to the increase in grain size and decrease in conductivity. An increase in grain size would increase the probability of hopping occurring between Fe, Co and Cu ions, resulting in an enhancement in dielectric constant. On the other hand, an increase in grain size would decrease the resistivity of the materials because of the resulting fewer grain boundaries, and that would also be beneficial for enhancing the dielectric constant and decreasing the dielectric loss tangent.

Conclusions

Single-phase cubic spinel structured $Co_{0.4}Cu_{0.1}Zn_{0.5}Dy_xFe_{2-x}O_4$ nanoparticles were successfully prepared using the sol–gel autocombustion route. The Dy substitution resulted in an increase in tensile strain in the materials from 3.1 ($x = 0.0$) to 4.3×10^{-4} ($x = 0.045$), consistent with the lattice length having increased from 8.340 to 8.545 Å. The average crystallite size increased from 39.5 to 41 nm with the Dy substitution. Zn^{2+} ions occupied the A site only; Co^{2+} and Dy^{3+} occupied the B site whereas Cu^{2+} and Fe^{3+} occupied both crystallographic sites. Force constants, elastic parameters and Debye temperatures increased with Dy substitution. Increases in grain size, magnetocrystalline anisotropy, and 4f–3d couplings and strengthening of the A–B interaction with the Dy substitution resulted in increases in all of the magnetic properties. Saturation magnetization increased from 21 to 38 emu g^{-1} whereas coercivity increased from 480 to 560 Oe with the increase in Dy substitution. The enhancement in saturation magnetization was also related to the higher magnetic moment of Dy ions compared to that of Fe ions. The dielectric constant increased from 355 to 2400, and dielectric loss also slightly decreased, when Dy was included. This ability to modify the magnetic properties of the prepared material makes it a suitable candidate for magnetic recording media.

Conflicts of interest

All the authors declare no conflict of interest.

Acknowledgements

References

1 S. E. Shirsath, D. Wang, S. S. Jadhav, M. L. Mane and S. Li, Ferrites obtained by sol-gel method, in *Handbook of Sol-Gel Science and Technology*, ed. L. Klein, M. Aparicio and A. Jitianu, Springer, Cham, 2018, pp. 695–735.

2 H. Kaur, A. Singh, V. Kumar and D. S. Ahlawat, Structural, thermal and magnetic investigations of cobalt ferrite doped with Zn^{2+} and Cd^{2+} synthesized by auto combustion method, *J. Magn. Magn. Mater.*, 2019, **474**, 505–511.

3 G. Mustafa, M. U. Islam, W. Zhang, Y. Jamil, A. W. Anwar, M. Hussain and M. Ahmad, Investigation of structural and magnetic properties of Ce^{3+} substituted nanosized Co–Cr ferrites for variety of applications, *J. Alloys Compd.*, 2015, **618**, 428.

4 A. Goldman, *Modern Ferrite Technology*, 2nd edn, Springer, 2006.

5 P. Jadoun, J. Sharma, S. Kumar, S. N. Dolia, D. Bhatnagar and V. K. Saxena, Structural and magnetic behavior of nanocrystalline Cr doped Co–Mg ferrite, *Ceram. Int.*, 2018, **44**, 6747.

6 S. E. Shirsath, R. H. Kadam, M. L. Mane, A. Ghesami, Y. Yasukawa, X. Liu and A. Morisako, Permeability and magnetic interactions in Co^{2+} substituted $Li_{0.5}Fe_{2.5}O_4$ alloys, *J. Alloys Compd.*, 2013, **575**, 145–151.

7 M. A. Amer, T. M. Meaz, A. G. Mostafa and H. F. El-Ghazally, Annealing effect on the structural and magnetic properties of the $CuAl_{0.6}Cr_{0.2}Fe_{1.2}O_4$ nano-ferrites, *Mater. Res. Bull.*, 2015, **67**, 207.

8 C. N. R. Rao, P. J. Thoma and G. U. Kulkarni, *Nanocrystals: Synthesis, Properties and Applications*, Springer-Verlag, Berlin Hiedelberg, 2007.

9 W. S. Mohamed, M. Alzaid, M. S. M. Abdelbaky, Z. Amghouz, S. García-Granda and A. M. Abu-Dief, Impact of Co^{2+} Substitution on Microstructure and Magnetic Properties of $Co_xZn_{1-x}Fe_2O_4$ Nanoparticles, *Nanomaterials*, 2019, **9**(11), 1602.

10 S. E. Shirsath, X. Liu, Y. Yasukawa, S. Li and A. Morisako, Switching of magnetic easy-axis using crystal orientation for large perpendicular coercivity in $CoFe_2O_4$ thin films, *Sci. Rep.*, 2016, **6**, 30074.

11 S. E. Shirsath, X. Liu, M. H. N. Assadi, A. Younis, Y. Yasukawa, S. Kumar Karan, J. Zhang, J. Kim, D. Wang, A. Morisako, Y. Yamauchi and S. Li, Au quantum dots engineered room temperature crystallization and magnetic anisotropy in $CoFe_2O_4$ thin films, *Nanoscale Horiz.*, 2019, **4**, 434–444.

12 D. R. Mane, D. D. Birajdar, S. Patil, S. E. Shirsath and R. H. Kadam, Redistribution of cations and enhancement in magnetic properties of sol-gel synthesized $Cu_{0.7-x}Co_xZn_{0.3}Fe_2O_4$ ($0 < x < 0.5$), *J. Sol. Gel Sci. Technol.*, 2011, **58**, 70.

13 M. Hashim, S. K. Alimuddin, B. H. Koo, S. E. Shirsath, E. M. Mohammed, J. Shah, R. K. Kotnala, H. K. Choi, H. Chung and R. Kumar, Structural, electrical and magnetic properties of Co-Cu ferrite nanoparticles, *J. Alloys Compd.*, 2012, **518**, 11–18.

14 W. S. Mohamed and A. M. Abu-Dief, Impact of rare earth europium (RE-Eu^{3+}) ions substitution on microstructural, optical and magnetic properties of CoFe$_{2-x}$Eu$_x$O$_4$ nanosystems, *Ceram. Int.*, 2020, **46**, 16196–16209.

15 S. R. Naik and A. V. Salker, Change in the magneto structural properties of rare earth doped cobalt ferrites relative to the magnetic anisotropy, *J. Mater. Chem.*, 2012, **22**, 2740–2750.

16 S. E. Shirsath, R. H. Kadam, S. M. Patange, M. L. Mane, A. Ghasemi and A. Morisako, Enhanced magnetic properties of Dy^{3+} substituted Ni-Cu-Zn ferrite nanoparticles, *Appl. Phys. Lett.*, 2012, **100**, 042407.

17 E. Rezlescu, N. Rezlescu, P. D. Mangeron, L. Rezlescu and C. Pasxick, The influence of R$_2$O$_3$ (R = Yb, Er, Dy, Tb, Gd, Sm, and Ce) on the electric and mechanical properties of a nickel–zinc ferrite, *Phys. Status Solidi A*, 1997, **162**, 673.

18 S. E. Shirsath, S. S. Jadhav, B. G. Toksha, S. M. Patange and K. M. Jadhav, Remarkable influence of Ce^{4+} ions on the electronic conduction of Ni$_{1-2x}$Ce$_x$Fe$_2$O$_4$, *Scr. Mater.*, 2011, **64**, 773–776.

19 M. A. Almessiere, Y. Slimani, A. D. Korkmaz, S. Güner, A. Baykal, S. E. Shirsath, I. Ercan and P. Kögerler, Sonochemical synthesis of Dy^{3+} substituted Mn$_{0.5}$Zn$_{0.5}$Fe$_{2-x}$O$_4$ nanoparticles: structural, magnetic and optical characterization, *Ultrason. Sonochem.*, 2020, **61**, 04836.

20 M. Hashim, A. Ahmed, S. A. Ali, S. E. Shirsath, M. M. Ismail, R. Kumar, S. Kumar, S. S. Meena and D. Ravinder, Structural, optical, elastic and magnetic properties of Ce and Dy doped cobalt ferrite, *J. Alloys Compd.*, 2020, **834**, 155089.

21 M. V. Chaudhari, S. E. Shirsath, A. B. Kadam, R. H. Kadam, S. B. Shelke and D. R. Mane, Site occupancies of Co-Mg-Cr-Fe ions and their impact on the properties of Co$_{0.5}$Mg$_{0.5}$Cr$_x$Fe$_{2-x}$O$_4$, *J. Alloys Compd.*, 2013, **552**, 443–450.

22 T. Tatarchuk, M. Myslin, I. Mironyuk, M. Bououdina, A. T. Pedziwiatr, R. Gargula, B. F. Bogacz and P. Kurzydlo, Synthesis, morphology, crystallite size and adsorption properties of nanostructured Mg-Zn ferrites with enhanced porous structure, *J. Alloys Compd.*, 2020, **819**, 152945.

23 B. D. Cullity, *Introduction to Magnetic Materials*, Addison-Wesley, Massachusetts, 1972.

24 R. H. Kadam, A. R. Biradar, M. L. Mane and S. E. Shirsath, Sol-gel autocombustion synthesis of Li$_{3x}$MnFe$_{2-x}$O$_4$ and their characterization, *J. Appl. Phys.*, 2012, **112**, 043902.

25 L. Weil, F. Bertaut and L. Bochirol, Propriétés magnétiques et structure de la phase quadratique du ferrite de cuivre, *J. Phys. Radium*, 1950, **11**, 208.

26 K. B. Modi, S. J. Shah, C. R. Kathad, D. K. Sonigra, H. P. Parmar and K. M. Jadhav, On the relationship between structural – elastic properties of Co-Zn ferrites at 300 K, *Adv. Mater. Res.*, 2016, **1141**, 147.

27 K. J. Standley, *Oxide magnetic materials*, Clarendon Press, Oxford, 1972.

28 J. W. Vrewey and E. L. Heilmann, Physical properties and cation arrangement of oxides with spinel structures I. Cation arrangement in spinels, *J. Chem. Phys.*, 1947, **15**, 174–180.

29 G. Fagherazzi and F. Garbassi, X-ray diffraction measurements of the cation distribution in spinel structures, *J. Appl. Crystallogr.*, 1972, **5**, 18–23.

30 R. H. Kadam, K. Desai, V. S. Shinde, M. Hashim and S. E. Shirsath, Influence of Gd^{3+} ions substitution on the MnCrFeO$_4$ for their nanoparticle shape formation and magnetic properties, *J. Alloys Compd.*, 2016, **657**, 487–494.

31 R. Valenzuela, *Magnetic ceramics*, Cambridge University Press, 1994.

32 K. Parikh, R. V. Upadhyay, L. Belova and K. V. Rao, Ternary monodispersed Mn$_{0.5}$Zn$_{0.5}$Fe$_2$O$_4$ ferrite nanoparticles: preparation and magnetic characterization, *Nanotechnology*, 2006, **17**, 5970–5975.

33 T. K. Pathak, N. H. Vasoya, V. K. Lakhani and K. B. Modi, Structural and magnetic phase evolution study on needle-shaped nanoparticles of magnesium ferrite, *Ceram. Int.*, 2010, **36**, 275–281.

34 R. H. Kadam, S. T. Alone, M. L. Mane, A. R. Birajdar and S. E. Shirsath, Phase evaluation of Li$^+$ substituted CoFe$_2$O$_4$ nanoparticles, their characterizations and magnetic properties, *J. Magn. Magn. Mater.*, 2014, **355**, 70.

35 R. Waldron, Infrared spectra of ferrites, *Phys. Rev.*, 1955, **99**, 1727.

36 A. A. Birajdar, S. E. Shirsath, R. H. Kadam, M. L. Mane and D. R. Mane, Permeability and magnetic properties of Al^{3+} substituted Ni$_{0.7}$Zn$_{0.3}$Fe$_2$O$_4$ nanoparticles, *J. Appl. Phys.*, 2012, **112**, 053908.

37 D. Boukkeze, J. Massoudi, W. Hzez, M. Smari, A. Bougoffa, K. Khirouni, E. Dhahri and L. Bessais, Investigation of the structural, optical, elastic and electrical properties of spinel LiZn$_2$Fe$_3$O$_8$ nanoparticles annealed at two distinct temperature, *RSC Adv.*, 2019, **9**, 40940.

38 K. B. Modi, S. J. Shah, N. B. Pujara, T. K. Pathak, N. H. Vasoya and I. G. Jhala, Infrared spectral evolution, elastic, optical and thermodynamic properties study on mechanically milled Ni$_{0.5}$Zn$_{0.5}$Fe$_2$O$_4$ spinel ferrite, *J. Mol. Struct.*, 2013, **1049**, 250.

39 M. B. Mohamed and A. M. Wahba, Structural, magnetic and elastic properties of nanocrystalline Al-substituted Mn$_{0.5}$Zn$_{0.5}$Fe$_2$O$_4$ ferrite, *Ceram. Int.*, 2014, **40**, 11773.

40 A. Bhaskar and S. R. Murthy, Effect of sintering temperature on the elastic properties of Mn(1%) added MgCuZn ferrites, *J. Magn. Magn. Mater.*, 2014, **355**, 100.

41 R. S. Yadav, I. Kuritka, J. Havlica, M. Hnatko, C. Alexander, J. Masilko, L. Kalina, M. Hajduchova, J. Rusnak and V. Enev, Structural, magnetic, elastic, dielectric and electrical properties of hot-press sintered Co$_{1-x}$Zn$_x$Fe$_2$O$_4$ (x = 0.0, 0.5) spinel ferrite nanoparticles, *J. Magn. Magn. Mater.*, 2018, **447**, 48–57.

42 S. A. Mazen, S. F. Mansour, E. Dhahri, H. M. Zaki and T. A. Elmosalami, The infrared absorption and dielectric properties of Li-Ga ferrite, *J. Alloys Compd.*, 2009, **470**, 294.

43 R. A. Pawar, S. M. Patange, A. R. Shitre, S. K. Gore, S. S. Jadhav and S. E. Shirsath, Crystal chemistry and single-phase synthesis of Gd^{3+} substituted Co-Zn ferrite nanoparticles for enhanced magnetic properties, *RSC Adv.*, 2018, **8**, 25258–25267.

44 V. Choudhari, R. H. Kadam, M. L. Mane, S. E. Shirsath, A. B. Kadam and D. R. Mane, Effect of La^{3+} impurity on magnetic and electrical properties of Co-Cu-Cr-Fe nanoparticles, *J. Nanosci. Nanotechnol.*, 2014, **14**, 1–8.

45 V. G. Patil, S. E. Shirsath, S. D. More, S. J. Shukla and K. M. Jadhav, Effect of zinc substitution on structural and elastic properties of cobalt ferrite, *J. Alloys Compd.*, 2009, **488**, 199.

46 M. B. Kothale, K. K. Patankar, S. L. Kadam, V. L. Mathe, A. V. Rao and B. K. Chougule, Dielectric behaviour and magnetoelectric effect in copper-cobalt ferrite + barium lead titanate composites, *Mater. Chem. Phys.*, 2002, **78**, 691.

47 J. C. Maxwell, *Electricity Magnetism*, Oxford University Press, Oxford, 1954, ch. 328, vol. 1.

48 K. W. Wagner, The distribution of relaxation times in typical dielectrics, *Ann. Phys.*, 1973, **40**, 817–819.

49 C. G. Koops, On the dispersion of resistivity and dielectric constant of some semiconductors at audiofrequencies, *Phys. Rev.*, 1951, **83**, 121.

50 N. Rezlescu and E. Rezlescu, Dielectric properties of copper containing ferrites, *Phys. Status Solidi*, 1974, **23**, 575.